






Second harmonic Hall responses of insulators as a probe of Berry curvature dipole

Mahmut Sait Okyay ^{1,6}, Shunsuke A. Sato ^{2,3}, Kun Woo Kim ⁴, Binghai Yan ⁵, Hosub Jin¹ & Noejung Park ¹✉

Diverse nonlinear optical responses of metallic band states have been characterized in terms of the Berry curvature dipole (BCD) or other multipole structures of Berry curvature. Here, we find that the second harmonic optical responses of insulators to sub-bandgap light are also delicately associated with the interband BCD. We performed real-time time-dependent density functional theory calculations and theoretically analyzed the second harmonic generation susceptibility tensors. The two-band term of the second-order susceptibility is precisely proportional to the interband BCD, which is particularly significant for low-symmetric systems with a small bandgap. We show that higher-order responses to nonperturbative strong fields can be associated with higher poles of Berry curvature. We suggest that the consequences of symmetry lowering can be detected by nonlinear optical responses through adjustments of the dipole or other multipole structures of the Berry curvature texture.

¹Department of Physics, Ulsan National Institute of Science and Technology (UNIST), Ulsan 44919, Republic of Korea. ²Center for Computational Sciences, University of Tsukuba, Tsukuba 305-8577, Japan. ³Max Planck Institute for the Structure and Dynamics of Matter, 22761 Hamburg, Germany. ⁴Department of Physics, Chung-Ang University, 06974 Seoul, Korea. ⁵Department of Condensed Matter Physics, Weizmann Institute of Science, Rehovot 7610001, Israel. ⁶Present address: Materials Science & Engineering Program, Department of Chemical & Environmental Engineering, University of California-Riverside, Riverside, CA 92521, USA. ✉email: noejung@unist.ac.kr

Many key discussions in recent studies of condensed matter physics have often focused on the geometrical structures of quantum mechanical wavefunctions of electronic band states. Among the prime attributes underlying such geometrical natures is the Berry curvature of the Bloch state¹. Earlier recognition of the significance of the Berry curvature was provided by Thouless, Kohmoto, Nightingale, and Nijs (TKNN). They proved that, even before Berry's original formulation of the geometrical phase, the transverse charge conductivity of a two-dimensional (2D) band insulator is quantized in terms of the zone-integrated Berry curvature². In parallel with the similar geometrical notions of the Landau level states in integer quantum Hall effects³, the TKNN's formulation for the nonzero integer multiples of the Hall conductivity has laid the foundation for the topological state of band electrons, in particular, for the solid state with broken time-reversal symmetry (TRS)^{2,4}. The topological notions have later extended even for the time-reversal symmetric solid states in the context of the quantum spin Hall states^{5–7} and the Weyl/Dirac semimetals, which is reminiscent of the relativistic massless particle with distinct helicities^{8,9}.

For a time-reversal symmetric system, there is no charge Hall current in the linear regime, and the zone integration of the Berry curvature vanishes because of its odd nature in the momentum space. Even under such a strong constraint of TRS, the effect of the Berry curvature is still appreciable in the nonlinear regime, and significant interests in recent years have focused on such nonlinear optical responses^{10,11}. As suggested by Sodemann and Fu in 2015¹² and as measured by Ma et al. in 2019¹⁰, an inversion-broken metallic solid exhibits a nonzero charge Hall effect in the second-order response, which can be associated with the Berry curvature dipole (BCD)—the integration of the gradient of Berry curvature. On the other hand, for insulators, to describe a circular photogalvanic effect (CPGE) in response to a circularly polarized photoexcitation^{11,13–17}, the concept of the interband BCD has been devised by the integration of the Berry curvature difference of two band-edge states over the surface with a given energy separation. It is noteworthy that the CPGE photoconductivity is quantized at nodes of Weyl semimetals in terms of interband BCD^{18,19}. The concept of the BCD has also been extended to discussions for the magnetoresistance of Weyl metals²⁰ and the orbital Edelstein effect²¹.

The interband photogalvanic effects under TRS, such as shift or injection currents, are available only when the light frequency is larger than the bandgap^{13,14,16}. On the other hand, the effect of sub-bandgap driving lights is appreciable only in oscillating nonlinear responses, such as the second harmonics or even higher harmonics signals. Note that the nonlinear Hall effect (NLHE) of metals or semimetals has attracted significant interest in recent days^{10–12}. Here, we are motivated by the question of whether such notions of the NLHE of metals, as formulated in terms of BCD, can be extended to the second harmonic optical responses of insulators with TRS. To examine the nonlinear Hall responses of insulators to light fields with a sub-bandgap frequency, we performed the real-time time-dependent density functional theory (rt-TDDFT) calculations for h-BN and WTe₂ monolayers with various spatial symmetry groups, which are all symmetric over the time-reversal. Our real-time calculations cover strong fields beyond the perturbative regime, and we compare the simulation results with the perturbation-based results for second harmonic generation (SHG) and other susceptibility^{13,22}. We show that the SHG susceptibility can be decomposed into two-band and three-band terms. For small bandgap and lower symmetry cases, the SHG signals are dominated mainly by the former term, which is proportional to the band-edge states' interband BCD. In short, our results indicate that the correlation between the Berry curvature derivatives and nonlinear

optical responses can be described within a unified picture, irrespective of metals or insulators. The transverse nonlinear optical responses of insulators are dominated by the BCD, which is precisely analogous to the NLHE of metallic systems.

Results and discussion

Second-order optical responses of insulators and nonlinear Hall effect of metals. Various optical responses of materials have usually been discussed in terms of dipole-approximated Hamiltonian²³: $\hat{H}(\hat{\mathbf{p}}, t) = \hat{H}(\hat{\mathbf{p}} + \frac{e}{c}\mathbf{A}(t)) \approx \hat{H}(\hat{\mathbf{p}}) + \frac{e}{mc}\hat{\mathbf{p}} \cdot \mathbf{A}(t)$, where the time-dependent vector potential $\mathbf{A}(t) = -c \int dt \mathbf{E}(t)$ describes the uniform electric field $\mathbf{E}(t)$ of the applied light and $\hat{\mathbf{p}}$ represents the canonical momentum operator¹³. For adiabatically evolving Bloch states, the momentum operator can be replaced with the velocity operator $\hat{\mathbf{p}}/m = \partial \hat{H}(\mathbf{k})/\hbar \partial \mathbf{k}$, where $\hat{H}(\mathbf{k})$ is the corresponding \mathbf{k} -resolved Hamiltonian. For insulators, the second-order effect of the dipole term produces plentiful optical responses, including injection current, shift current, SHG, optical rectification, and electro-optic effect^{13,14}. The shift current contains a net direct current (DC) upon the absorption of a photon, which presents substantial potential in terms of applications to photovoltaic devices. The injection current has been discussed in the framework of the CPGE, which is characterized by the generation of a constant DC rate on the absorption of a circularly polarized photon (see Fig. 1a). To make a better comparative analogy, the shift current DC response is sometimes called interband linear photogalvanic effect (LPGE), as opposed to the CPGE^{16,17}.

The material symmetry determines the current direction for both shift and injection currents. For the nonlinear responses of metallic systems, the second-order effect has recently attracted substantial attention from the perspective of the NLHE, which has also been referred to as intraband LPGE¹⁶ (see Fig. 1b). This NLHE of the time-reversal symmetric system is particularly attractive when one considers the fact that the linear regime Hall current occurs only in the system with broken TRS^{2,10,12,16}. The previous semiclassical study has neatly proved the association of this metallic NLHE with the BCD on the Fermi surface¹². Here, we confirm that the SHG of a time-reversal invariant insulator is also linked to its BCD. In literature, the CPGE has been considered as a probe of band-resolved Berry curvature; the LPGE and SHG have been associated with the shift vector, the Berry connection differences between the occupied and unoccupied bands^{17,24,25}. Our results in the present work signify that among this family of nonlinear responses, the SHG of insulators is also governed by Berry curvature of the band-state wavefunction.

We specify the notations for the intraband and interband Berry curvatures to present consistent formulations of these nonlinear optical responses. With the given energy band structure $\varepsilon_n(\mathbf{k})$ and the eigenstates $|\psi_n(\mathbf{k})\rangle$ of the static Hamiltonian $\hat{H}(\mathbf{k})$ for the Bloch state with the momentum vector \mathbf{k} , the band Berry curvature of the band index n can be written as

$$\Omega_n(\mathbf{k}) = 2\text{Im} \sum_{m \neq n} \frac{v_{nm}^y v_{mn}^x}{\omega_{mn}^2} \quad (1)$$

where $v_{nm}^\alpha = \langle \psi_n(\mathbf{k}) | \partial \hat{H}(\mathbf{k}) / \hbar \partial k_\alpha | \psi_m(\mathbf{k}) \rangle$ represent the velocity matrix elements between bands n and m , and $\omega_{mn} = [\varepsilon_m(\mathbf{k}) - \varepsilon_n(\mathbf{k})]/\hbar$. On the other hand, the velocity matrices between the bands n and m have been referred to as the interband Berry curvature¹⁵, which can be written as

$$\Omega_{nm}(\mathbf{k}) = 2\text{Im} \frac{f_{nk}(1 - f_{mk})v_{nm}^y v_{mn}^x}{\omega_{mn}^2} \quad (2)$$

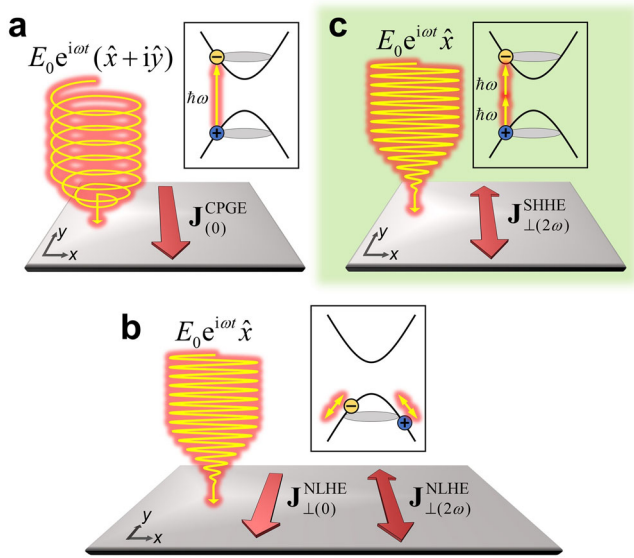


Fig. 1 The second-order optical effects of materials. **a** The circular photogalvanic effect (CPGE): applied circularly polarized light of energy $\hbar\omega$ and field strength E_0 (yellow lines) excites electron and hole carriers (yellow and blue balls in the inset). It induces a non-oscillating direct current ($\mathbf{J}_{(0)}^{\text{CPGE}}$) (thick brown arrow) in inversion-asymmetric materials. **b** The nonlinear Hall effect (NLHE) of metals: applied linear polarized (in the x -direction) light of frequency ω induces 2ω alternating current ($\mathbf{J}_{\perp(2\omega)}^{\text{NLHE}}$) together with a direct current ($\mathbf{J}_{\perp(0)}^{\text{NLHE}}$) in the transverse direction (the y -direction). **c** The second harmonic Hall effect (SHHE) of insulators: applied linear polarized (in the x -direction) light of frequency ω excites electron-hole pairs, generating 2ω alternating current ($\mathbf{J}_{\perp(2\omega)}^{\text{NLHE}}$) in the transverse direction (the y -direction).

where f_{nk} indicates the occupation factor. Note that the factor $f_{nk}(1-f_{mk})$ makes the interband Berry curvature becomes nonzero only between the pairs of occupied (n) and unoccupied (m) states. This form of the Berry curvature has been introduced to describe the CPGE of insulators^{11,15}.

Second harmonic Hall effect of two-dimensional insulators.

We now take an example 2D insulator to study the nonlinear optical response characteristics of insulators with TRS. We first search the solution, as depicted in Fig. 1c, by investigating the Fourier components of the transverse real-time current $\mathbf{J}_{\perp}(t)$ (in the y -direction) in response to a given driving field $\mathbf{E}(t) = E(t)\hat{\mathbf{x}} = E_0\text{Re}[e^{i\omega t}]\hat{\mathbf{x}}$ oscillating in the x -direction with a frequency smaller than the bandgap: $\hbar\omega < \epsilon_{\text{gap}}$. Since the sub-bandgap light does not activate the DC response, the only available second-order response can be found in the SHG spectra^{13,14}. In later paragraphs, we discuss that these second-order transverse optical responses can be formulated in an exact analogy with the NLHE^{10–12}. Without loss of generality, the transverse electric polarization can be written as $P_y(t) = -\chi^{(2)}E_0^2\text{Im}[e^{i2\omega t}]$, of which the corresponding current can be obtained by $J_y(t) = \dot{P}_y(t) = -2\omega\chi^{(2)}E_0^2\text{Re}[e^{i2\omega t}]$, where $\chi^{(2)} \equiv \text{Im}[\chi^{\text{yxx}}(-2\omega; \omega, \omega)]$ is the imaginary part of the SHG susceptibility¹³. Hereafter, this frequency-doubled transverse response of insulators is called the second harmonic Hall effect (SHHE).

Real-time profiles of the charge oscillations of the insulating materials were obtained through the rt-TDDFT calculations. The Kohn–Sham (KS) wavefunctions for the Bloch states $|\psi_{nk}(\mathbf{r}, t)\rangle$ evolves by the time-dependent density functional

Hamiltonian, as follows:

$$i\hbar\frac{\partial}{\partial t}|\psi_{nk}(\mathbf{r}, t)\rangle = \left[\frac{1}{2m_e} \left(\hat{\mathbf{p}} + \frac{e}{c}\mathbf{A}(t) \right)^2 + \hat{V}_{\text{atom}} + \hat{V}_{\text{Hxc}}[\rho(\mathbf{r}, t)] \right] |\psi_{nk}(\mathbf{r}, t)\rangle \quad (3)$$

The second and third terms on the right-hand side are the atomic pseudopotential and the Hartree-exchange-correlation potential, respectively. Further details for the computations of the time series of the wavefunctions are described in the Method section. The time profile of the cell-averaged current density can be calculated from the velocity expectation of the time-evolving KS wavefunctions $|\psi_{nk}(\mathbf{r}, t)\rangle$:

$$\mathbf{J}(t) = -\frac{e}{Lm} \sum_{nk} f_{nk} \langle \psi_{nk}(\mathbf{r}, t) | \hat{\boldsymbol{\pi}} | \psi_{nk}(\mathbf{r}, t) \rangle \quad (4)$$

where L is the average length of the 2D unit cell across the plane perpendicular to the current flow direction. The velocity operator in this nonlocal pseudopotential scheme is given by $\hat{\boldsymbol{\pi}} = \hat{\mathbf{p}} + \frac{e}{c}\mathbf{A}(t) + \frac{i\hbar m}{\hbar}[\hat{V}_{\text{NL}}, \hat{\mathbf{r}}]$, as elaborated in the previous literature⁷, where \hat{V}_{NL} represents the nonlocal part of the pseudopotential.

We traced the real-time dynamics of the transverse current density ($\mathbf{J}_{\perp}(t)$) of pristine monolayer h-BN with D_{3h} point group symmetry (see Fig. 2a) and strained h-BN (B–N bond lengths are elongated by 0.2 Å in the y -direction) with C_{2v} symmetry (see Fig. 2b). First, the pristine h-BN is driven by the x -polarized electric field $\mathbf{E}(t) = f(t)E_0 \cos(\omega_0 t)\hat{\mathbf{x}}$, which is perpendicular to the mirror plane \mathbf{M}_x . We set $E_0 = 0.005 \text{ V \AA}^{-1}$ and $\hbar\omega_0 = 2.37 \text{ eV}$, which corresponds precisely to half the bandgap (see the upper panel of Fig. 2c). Once the real-time profile of the transverse current $\mathbf{J}_{\perp}(t)$ is obtained within the [20 fs, 60 fs] range (the black arrowed line in the lower panel of Fig. 2c), we squared the Fourier coefficients, $|\mathbf{F}[\mathbf{J}_{\perp}(t)]|^2$, up to the fourth harmonic order of the applied frequency, as presented in Fig. 2d. The transverse current, $J_{\perp} = J_y$, exhibits a very sharp second harmonic peak at $2\omega_0$. In contrast, the other harmonic orders are negligible. However, when the polarization of the applied field is in the same plane as the mirror (when the \mathbf{E} is polarized into the y -direction of Fig. 2a, b), the transverse response current is negligible (see the green lines in Fig. 2c, d). This polarization-dependent charge oscillation is consistent with the cancellation of the transverse harmonic responses owing to the oddness of the Berry curvature over the mirror reflection^{26,27}. Overall, the high harmonics responses are considered manifestations of broken symmetry. For example, given the TRS, inversion breaking is necessary for even-order harmonics responses. Our present work establishes the connection between the effect of symmetry breaking with the underlying intrinsic band geometric properties, the Berry curvature texture, which microscopically accounts for the polarization-dependent SHGs.

We collected the SHG yield with respect to various sub-bandgap light frequencies, as depicted in Fig. 2e, f. For a 2D insulator, the imaginary part of the SHG susceptibility tensor $\chi^{(2)}$ in the sub-bandgap regime is given by ref. 13

$$\begin{aligned} \chi^{(2)}(\omega) &= \frac{2\pi e^2}{\hbar^2} \int_{\mathbf{k}} \sum_{nmp} \frac{(f_{nk} - f_{mk})^y v_{nm}^x v_{mp}^x v_{pn}^x + v_{mp}^y v_{pn}^y}{\omega_{mn}^3 (\omega_{mp} + \omega_{np})} [\delta(\omega_{mn} - 2\omega) - \delta(\omega_{mn} + 2\omega)] \\ &= -\frac{8\pi e^2}{\hbar^2} \int_{\mathbf{k}} \text{Im} \sum_{nmp} \frac{f_{nk}(1-f_{mk})^y v_{nm}^x v_{mp}^x v_{pn}^x}{\omega_{mn}^3 (\omega_{mp} + \omega_{np})} \delta(2\omega - \omega_{mn}) \text{ for } 2\hbar\omega > \epsilon_{\text{gap}} > \hbar\omega \end{aligned} \quad (5)$$

where ϵ_{gap} is the bandgap energy of the insulator and $\int_{\mathbf{k}} = \int_{\frac{d^2\mathbf{k}}{4\pi^2}}$ stands for the 2D Brillouin zone integration. The sum of each (m, n) and (n, m) pairs in the first line of Eq. (5) results in twice the

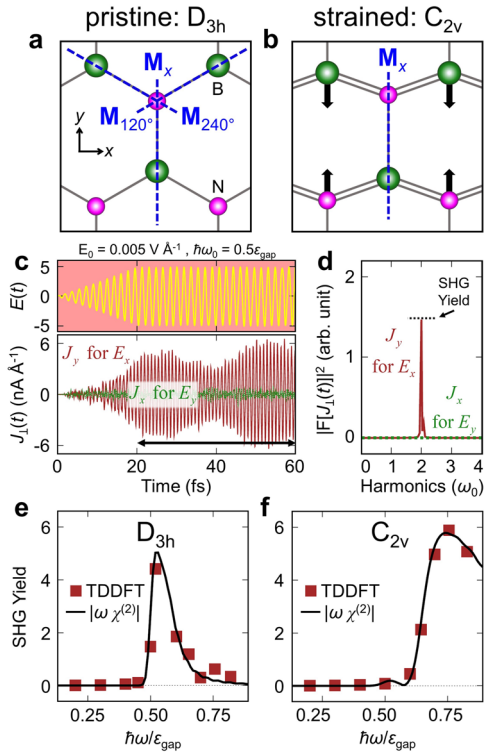


Fig. 2 The second harmonic Hall current spectra in h-BN. **a** and **b** are the top views of the three-fold D_{3h} symmetric pristine and the two-fold C_{2v} symmetric uniaxial strained h-BN monolayers, respectively. The blue dashed lines represent the mirror planes: M_x is perpendicular to the x -axis; M_{120° and M_{240° are obtained by rotating the M_x plane clockwise 120° and 240° around the z -axis, respectively. The upper plane of **c** is the real-time profile of the continuous light field applied to the pristine h-BN. The solid brown and dotted green oscillating lines in the lower plane are the transverse current density responses obtained by the real-time time-dependent density functional theory (TDDFT) calculations with the polarization of the applied field in the x -axis and y -axis, respectively. **d** The Fourier transformation of the current densities given in **c** for the time interval of $20 \text{ fs} \leq t \leq 60 \text{ fs}$ (the black horizontal arrowed line). The horizontal dashed line depicts the second harmonic generation (SHG) yield. **e** The SHG yields obtained from TDDFT (brown squares) and the theoretical SHG susceptibility spectra (black lines) for the pristine h-BN (with D_{3h} symmetry) with respect to various driving frequencies. **f** The same plots as **e** for a strained h-BN (with C_{2v} symmetry). The light frequency in the horizontal axis is normalized with the bandgap of each structure (4.75 eV for D_{3h} and 3.61 eV for C_{2v}).

imaginary part of the summand in the second line. For a side remark, this form is valid only for time-reversal symmetric systems, and time-reversal breaking brings many other competing terms besides the form written in Eq. (5)^{28,29}. Here, we compare this second harmonic susceptibility, which is based on the second-order perturbation theory, with the Fourier transform of the ab initio real-time current profile. Figure 2e, f demonstrates a good coincidence between the total SHG susceptibility spectra $|\omega \chi^{(2)}|$ and the SHG yield obtained from the rt-TDDFT calculations in the examples of the h-BN structures. Note that, in the ab initio rt-TDDFT calculations, the real-time profiles are directly integrated over time, and thus we do not have to consider whether the field is strong or weak. For the results shown in Fig. 2e, f, which seemingly belong to the perturbative regime, both methods confirm that the transverse response becomes significant when the light frequency exceeds one-half the bandgap. This can be attributed to the two-photon excitation nature in the nonlinear

regime. As seen from Fig. 2e, f, the SHG intensities computed with the TDDFT calculation are accurately reproduced only by the imaginary part of $\chi^{(2)}$. This indicates that the imaginary part dominates the SHG response in the resonant condition as it relies on the resonant nonlinear processes, in which the contribution of the real part remains marginal.

Interband BCD and second harmonic Hall effect. The intra-band BCD has been widely cited as a key descriptor for the NLHE of metallic Fermi surfaces^{12,16,30}. Analogously, the interband BCD has recently been defined for CPGE of insulating bands that are separated by the photon energy of the incident light^{11,15}. Here, we propose that the SHHE (the second harmonic Hall response of insulators to the sub-bandgap driving field) can be described by the interband BCD in exact analogy with the NLHE of metals formulated by intraband BCD. The interband BCD can be defined by the pair of the band-edge states (one occupied and one unoccupied) as follows:

$$D_{vc}(\omega) = \int_{\mathbf{k}} \frac{\partial \Omega_{vc}}{\partial \mathbf{k}} \Theta(2\omega - \omega_{cv}) \quad (6)$$

where v and c indicate a valence band and a conduction band state, respectively. Θ represents the Heaviside step function¹⁵. Ω_{vc} is defined in Eq. (2). When the band-edge states are well separated from others, only the valence band maxima (VBM) and conduction band minima (CBM) can be selected, constituting the two-band approximation^{11,15}.

Throughout the NLHE, CPGE, and SHHE, all the effects of the material's symmetry can be discussed in terms of the corresponding BCD. For example, when the system has reflection symmetry with respect to the M_x mirror plane, the derivatives of both the intraband and interband Berry curvature must keep the relations $\frac{\partial \Omega}{\partial k_y} \Big|_{(-k_x, k_y)} = -\frac{\partial \Omega}{\partial k_y} \Big|_{(k_x, k_y)}$ and $\frac{\partial \Omega}{\partial k_x} \Big|_{(-k_x, k_y)} = \frac{\partial \Omega}{\partial k_x} \Big|_{(k_x, k_y)}$ because the Berry curvature is an odd function under M_x mirror reflection, $\Omega(-k_x, k_y) = -\Omega(k_x, k_y)$. This indicates that the momentum derivative of the Berry curvature possesses the pseudo-vector nature, the perpendicular component is even, and the in-plane component is odd with respect to the mirror reflection. As a result, the interband BCD, given in Eq. (6), must be perpendicular to the mirror plane M_x . Because of this pseudo-vector nature, the presence of additional mirror planes makes the BCD vanish^{10-12,31}. The step function dictates that the x -component of $D_{vc}(\omega)$ also vanishes when the light frequency is below $0.5\epsilon_{\text{gap}}$.

Now, we decompose the SHG susceptibility tensor given in Eq. (5) into two parts: $\chi^{(2)} = \chi_{2\text{-band}}^{(2)} + \chi_{3\text{-band}}^{(2)}$, where $\chi_{2\text{-band}}^{(2)}$ counts the terms only when $p = m$ or $p = n$, and $\chi_{3\text{-band}}^{(2)}$ stands for all the other terms. The two terms can be explicitly written as

$$\chi_{2\text{-band}}^{(2)}(\omega) = \frac{8\pi e^3}{\hbar^2} \int_{\mathbf{k}} \text{Im} \sum_{nm} \frac{f_{nk}(1-f_{mk})v_{nm}^y v_{mn}^x}{\omega_{mn}^4} \Delta v_{mn}^x \delta(2\omega - \omega_{mn}) \quad (7)$$

$$\chi_{3\text{-band}}^{(2)}(\omega) = -\frac{8\pi e^3}{\hbar^2} \int_{\mathbf{k}} \text{Im} \sum_{nmp} \frac{f_{nk}(1-f_{mk})v_{nm}^y v_{mp}^x v_{pn}^x}{\omega_{mn}^3(\omega_{mp} + \omega_{np})} \delta(2\omega - \omega_{mn}) \quad (8)$$

where $\Delta v_{mn}^x = v_{mm}^x - v_{nn}^x$ are the velocity expectation differences between the bands m and n at the Bloch point \mathbf{k} . Using the definition of the interband Berry curvature and the identity $\Delta v_{mn}^x = \frac{d\omega_m}{dk_x} - \frac{d\omega_n}{dk_x} = \frac{d\omega_{mn}}{dk_x}$, one can reduce $\chi_{2\text{-band}}^{(2)}$ to the summation of interband BCD for all pairs of occupied (n) and

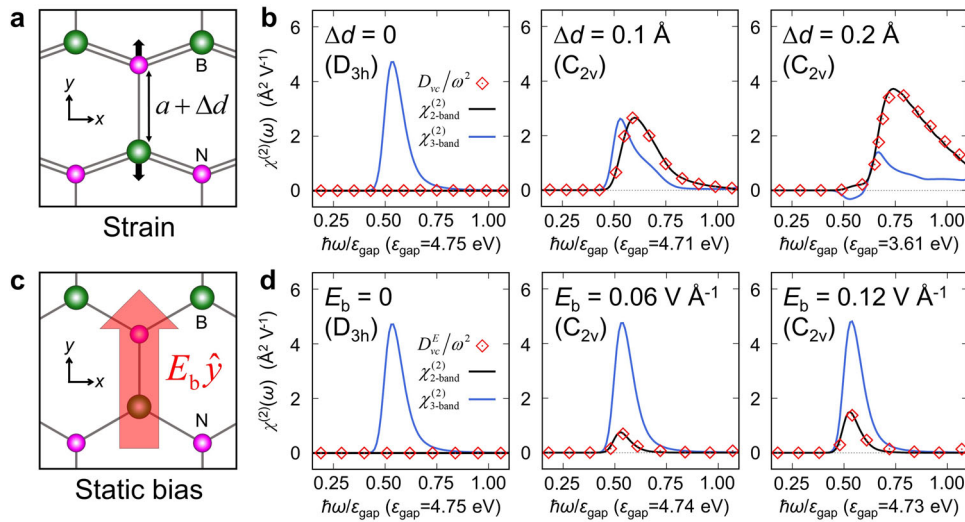


Fig. 3 The two-band and three-band contributions to the second harmonic generation (SHG) susceptibility compared with the interband Berry curvature dipole (BCD). **a** The monolayer h-BN, in which the B-N bond lengths are extended by Δd in the y -direction. The single (double) lines represent the long (short) bonds of the strained h-BN. **b** The comparison of 2-band and 3-band transition terms of SHG susceptibility spectra with the interband BCD for gradually increasing Δd values. **c** The un-strained h-BN, whose symmetry is adjusted by the static electric field bias of strength E_b in the y -direction (the thick red arrow). **d** The same as **b** with varying E_b values.

unoccupied (m) bands as

$$\chi_{2\text{-band}}^{(2)}(\omega) = \frac{\pi e^3}{\hbar^2 \omega^2} \sum_{nm} (\mathbf{D}_{nm} \cdot \hat{\mathbf{x}}) \quad (9)$$

This expression establishes the relation between the SHG signals and the interband BCD. The detailed derivation of Eq. (9) is given in Supplementary Note 1. The denominator in Eq. (7) indicates that the dominant contribution to Eq. (9) comes from the band-edge pair. In particular, when the band edge states are well separated from the other bands, the two-band term can be effectively approximated as

$$\chi_{2\text{-band}}^{(2)}(\omega) \approx \frac{\pi e^3}{\hbar^2 \omega^2} (\mathbf{D}_{vc} \cdot \hat{\mathbf{x}}) \quad (10)$$

where \mathbf{D}_{vc} represents the interband BCD of the band-edge pair. Since \mathbf{D}_{vc} is perpendicular to the mirror plane, $\chi_{2\text{-band}}^{(2)}$ also preserves the same symmetry constraints and vanishes in the presence of multiple reflection symmetries. On the other hand, $\chi_{3\text{-band}}^{(2)}$ cannot be reduced to such a pseudo-vector form, and it is even under the mirror reflection by an even number of ν^x integrations. Thus, $\chi_{3\text{-band}}^{(2)}$ is not required to vanish by additional mirror planes in three-fold symmetric point groups.

The calculated results of $\chi_{2\text{-band}}^{(2)}$, $\chi_{3\text{-band}}^{(2)}$, and \mathbf{D}_{vc}/ω^2 with various driving frequencies for the h-BN monolayers are presented in Fig. 3. To alter the symmetry of the h-BN, from that of three-fold (D_{3h}) to two-fold (C_{2v}), one of the bonds is elongated as depicted in Fig. 3a, b or a static electric field is applied along the y -direction as presented in Fig. 3c, d. The former is a simple geometric change, while the symmetry breaking for the latter is achieved by the inclusion of the bias field. To take the symmetry lowering effect into account, one needs to obtain the dipole of the field-induced Berry curvature, Ω_{vc}^E , which can be calculated using the Berry connection polarizability (BCP) tensor³². The BCP has been introduced in the studies for the second-order anomalous Hall effect of ferromagnets^{33,34}, and the third-order NLHE of time-reversal invariant materials^{35,36}. The induced interband Berry curvature

under a static electric bias $E_b \hat{y}$ can be obtained by

$$\Omega_{vc}^E(\mathbf{k}) = E_b \left[\frac{\partial C_{vc}^{yy}}{\partial k_x} - \frac{\partial C_{vc}^{xy}}{\partial k_y} \right] \quad (11)$$

where $G_{vc}^{ab}(\mathbf{k}) = -2e \text{Re}\{v_{vc}^a v_{cv}^b / \omega_{cv}^3\}$. The corresponding BCD, $\mathbf{D}_{vc}^E(\omega) = \int_{\mathbf{k}} \frac{\partial \Omega_{vc}^E}{\partial \mathbf{k}} \Theta(2\omega - \omega_{cv})$, is displayed in Fig. 3d for various bias fields. Note that the two-band term of the SHG susceptibility tensor, $\chi_{2\text{-band}}^{(2)}$, is well matched with \mathbf{D}_{vc}/ω^2 and $\mathbf{D}_{vc}^E/\omega^2$, as depicted in Fig. 3b, d, which supports our derivation in Eq. (10). This coincidence also suggests that the BCD is dominantly contributed by the band-edge pairs, and the contribution from other bands, away from the band edges, are negligible.

The two-band contribution, $\chi_{2\text{-band}}^{(2)}$, inherits the same symmetry constraint of BCD. The three-fold D_{3h} point group possesses three vertical mirror planes, as depicted in Fig. 2a, which makes the BCD, and hence the $\chi_{2\text{-band}}^{(2)}$, vanish as presented in the leftmost panels of Fig. 3b, d. However, the three-band term, $\chi_{3\text{-band}}^{(2)}$, is not constrained by symmetry. Thus the SHG response produced in the noncentrosymmetric insulator with more than one mirror plane is solely attributable to $\chi_{3\text{-band}}^{(2)}$. This response has recently been explained in terms of skew scattering through the Berry curvature triple, a higher-order moment of the Berry curvature³⁷.

To explicitly demonstrate the effect of symmetry, we applied a uniaxial strain (Fig. 3a, b), lifting the two mirror planes of the D_{3h} point group. By straining the structure into the C_{2v} point group, the contribution from the two-band term, $\chi_{2\text{-band}}^{(2)}$, is gradually increased, dominating over the three-band term, $\chi_{3\text{-band}}^{(2)}$. The most significant contribution to the summation in Eq. (7) and Eq. (8) comes from the smallest denominator, which scales as ω_{cv}^4 and ω_{cv}^3 for $\chi_{2\text{-band}}^{(2)}$ and $\chi_{3\text{-band}}^{(2)}$, respectively. As the bandgap decreases, the contribution from the $\chi_{2\text{-band}}^{(2)}$ becomes more significant, as summarized in Fig. 3b. For comparison, we tested a different method of symmetry adjustment: application of a uniform static in-plane electric bias (Fig. 3c, d). The effect of the static electric field is moderate compared with the geometric strain, and the bandgap variation is very marginal. In this case,

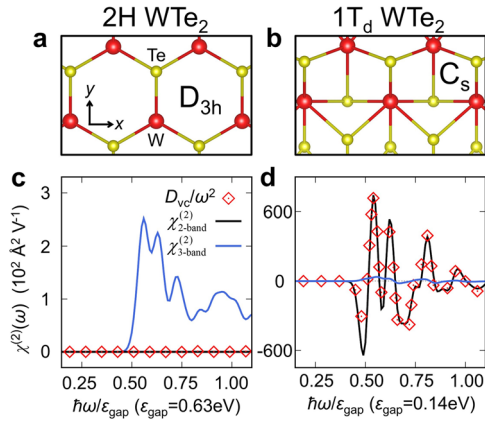


Fig. 4 The second harmonic Hall response of two polymorphs of monolayer WTe_2 . **a** The schematic for the 2H phase of WTe_2 with D_{3h} point group symmetry. **b** The schematic for the $1T_d$ phase of WTe_2 with a two-fold symmetric C_s point group. **c** The contributing terms to second harmonic generation susceptibility spectra (solid lines) and the interband Berry curvature dipole (red diamonds) for the 2H phase of WTe_2 . **d** The same for the $1T_d$ phase.

the contribution $\chi_{2\text{-band}}^{(2)}$ and $\mathbf{D}_{vc}^E/\omega^2$ turned on in proportion to the field strength, while those of $\chi_{3\text{-band}}^{(2)}$ are negligibly affected. This indicates that symmetry lowering mainly affects the BCD in these cases of insulators. It is noteworthy that the effect of symmetry lowering is also effective on the BCD of metallic bands, which has recently been discussed in the context of NLHE³⁸.

Instead of intentionally adjusting the symmetry by applying strain or external field, here we examine the effect of symmetry lowering and bandgap change by comparing two distinct polymorphs of existing materials: the 2H phase (D_{3h}) and the $1T_d$ phase (C_s) of WTe_2 monolayers (see Fig. 4a, b). The leading component in the summation in Eqs. (7) and (8) come from the band-edge pairs (the VBM and CBM). When the bandgap is small, and the band-edge states are well separated from other bands, the contribution of $\chi_{2\text{-band}}^{(2)}$ becomes dominant. Note that, in the extreme two-band limit, the response is wholly governed by the BCD term, that is $\chi_{2\text{-band}}^{(2)}$ ¹¹. The $1T_d$ phase of WTe_2 has a substantially smaller bandgap compared with the 2H phase, and the corresponding optical responses are two orders of magnitude larger than those of the 2H phase, as presented in Fig. 4c, d. The rapid sign change and cusp in Fig. 4d are due to the spin structure of the band edge states. The $1T_d$ phase of WTe_2 is a quantum spin Hall insulator, and the indirect band inversion at the band edge causes the Berry curvature of opposite spin states to have opposite signs. The peaks are attributable to the joint density of states between the band pairs of each spin state. Because of the spin-orbit coupled band splitting, the peaks contributed by the spin-up states locate at distinct energy points than those of spin-down states, resulting in the rapidly oscillatory feature shown in Fig. 4d.

As presented in Fig. 4d, the total SHG response, $\chi^{(2)}$, is almost identical to the two-band approximated BCD term, \mathbf{D}_{vc}/ω^2 , with a negligible contribution from the three-band term $\chi_{3\text{-band}}^{(2)}$. This evidences that the SHG signals of the narrow-gap insulators with the single mirror plane mainly originate from the interband BCD of the band-edge states. In this limit of two-band approximation, the SHHE current response can be summarized as^{10–12}

$$\mathbf{J}_\perp(t) = -\frac{2\pi e^3}{\hbar^2 \omega} \hat{\mathbf{z}} \times \mathbf{E}(\mathbf{D}_{vc} \cdot \mathbf{E}) \quad (12)$$

As confirmed by the rt-TDDFT calculation, presented in Fig. 2c, d, the SHHE response current is maximized when the

light is polarized along the BCD direction. All the results, shown in Figs. 3 and 4, suggest that the ratio between the contribution from the $\chi_{2\text{-band}}^{(2)}$ and the $\chi_{3\text{-band}}^{(2)}$ can be adjusted by controlling the material symmetry, which implies that the spectroscopy based on the transverse SHG signal can be utilized to detect the Berry curvature distribution together with the material orientation. More rigorous discussions of the effect of mirror and inversion symmetry on the band structure and Berry curvature distribution are given in Supplementary Note 3, based on the parametrized two-band model Hamiltonian, specified in Supplementary Note 2.

The SHHE under strong fields: the effect of Berry curvature multipoles.

We now examine the features of Hall responses under strong driving fields. In line with the nonlinear Hall response of the metallic system, in which the higher-order response current is associated with the intraband Berry curvature multipoles³⁹, here we examine whether the SHHE of the insulator, induced by a strong field, reflects the effect of multipoles of interband Berry curvature. In practice, the strong fields beyond the perturbative regime often cause diverse non-adiabatic effects, and the narratives based on band intrinsic quantity tend to be irrelevant. However, when the two-band approximation is robustly validated, and when the time scale of the driving oscillator is much faster than that of carrier relaxation dynamics, $2\pi/\omega \ll \tau$, the intrinsic band natures are adiabatically preserved even under the strong field. As the mirror plane is perpendicular to the x -axis in the coordinate specified in Fig. 2b, the band-edge BCD, \mathbf{D}_{vc} , is directed to the x -axis. The second harmonic Hall current in the y -direction induced by the field $\mathbf{E} = E_0 \text{Re}[e^{i\omega t}] \hat{\mathbf{x}}$ can be obtained from Eq. (12) as

$$J_y(t) = -\frac{2\pi e^3}{\hbar^2 \omega} E_0^2 \text{Re}[e^{i2\omega t}] \int_{\mathbf{k}} \frac{\partial \Omega_{vc}}{\partial k_x} \Theta(2\omega - \omega_{cv}) \quad (13)$$

Within this adiabatic approximation, the fast intraband motion of the carriers follows the acceleration rule $\mathbf{k} \rightarrow \mathbf{k} + \frac{e}{\hbar c} \mathbf{A}(t)$ with $\mathbf{A}(t) = -\frac{e}{\omega} E_0 \text{Im}[e^{i\omega t}] \hat{\mathbf{x}}$, which causes the deformation of the integration surface in Eq. (13). This change caused by the driven state of the momentum can be counted by substituting the integrand: $\frac{\partial \Omega_{vc}}{\partial k_x} \rightarrow \frac{\partial \Omega_{vc}}{\partial k_x} \Big|_{\mathbf{k} + \Delta \mathbf{k}}$ with $\Delta \mathbf{k}(t) = -\frac{e}{\hbar \omega} E_0 \text{Im}[e^{i\omega t}]$. Now, we expand the BCD with respect to $\Delta \mathbf{k}$, and the sum for each Kramers pair (\mathbf{k} and $-\mathbf{k}$) as:

$$\begin{aligned} \left. \frac{\partial \Omega_{vc}}{\partial k_x} \right|_{\mathbf{k} + \Delta \mathbf{k}} + \left. \frac{\partial \Omega_{vc}}{\partial k_x} \right|_{-\mathbf{k} + \Delta \mathbf{k}} &= 2 \frac{\partial \Omega_{vc}}{\partial k_x} + 2 \frac{1}{2!} \frac{\partial^3 \Omega_{vc}}{\partial k_x^3} (\Delta k)^2 \\ &+ 2 \frac{1}{4!} \frac{\partial^5 \Omega_{vc}}{\partial k_x^5} (\Delta k)^4 + \dots, \end{aligned} \quad (14)$$

where all the odd-order terms vanish by the odd symmetry of Ω_{vc} with respect to the mirror plane. Since the second harmonic oscillation in Eq. (13) is represented by $\text{Re}[e^{i2\omega t}]$, only the zero-frequency terms of the BCD expansion must be collected from those even-order terms of $(\Delta k)^2$, $(\Delta k)^4$, ... of Eq. (14) for the SHHE response. The second harmonic contribution to Eq. (13) can then be written as

$$J_y(t) = -\text{Re}[e^{i2\omega t}] \left\{ \frac{2\pi e^3}{\hbar^2 \omega} E_0^2 \mathbf{D}_{vc}^{(2)} + \frac{\pi e^5}{\hbar^4 \omega^3} E_0^4 \mathbf{D}_{vc}^{(4)} + \frac{7\pi e^7}{192 \hbar^6 \omega^5} E_0^6 \mathbf{D}_{vc}^{(6)} + \dots \right\} \cdot \hat{\mathbf{x}} \quad (15)$$

where $\mathbf{D}_{vc}^{(2)} = \mathbf{D}_{vc}$ and $\mathbf{D}_{vc}^{(n)}(\omega) = \int_{\mathbf{k}} \frac{\partial^{(n-1)} \Omega_{vc}}{\partial \mathbf{k}^{(n-1)}} \Theta(2\omega - \omega_{cv})$ are interband BCD and interband Berry curvature n th pole of the band-edge states, respectively. This expansion shows that the direct correspondence between the SHG responses and BCD is

limited only to weak fields. The strong field can bring higher-order contributions that can be formulated with the Berry curvature multipoles. Not only this second-order Hall responses, but the first-order susceptibility $\chi^{(1)}$, also contains similar second harmonic terms associated with Berry curvature multipoles within a similar semiclassical approach (see Supplementary Note 4). A few remarks are in order. Beyond the two-band approximations, in practice, particularly for the terms related to the $\chi_{3\text{-band}}^{(2)}$, the higher-order corrections are not limited to the multipoles of interband Berry curvatures. In recent studies, nonlinear optical responses are interpreted geometrically with higher rank tensors on the manifolds of Bloch cell periodic functions⁴⁰. This part of our analysis is introduced to guide only the intuitional picture for a nonperturbative strong-field regime. One must consider additional perturbative contributions to the second harmonic Hall responses^{40–42}, besides those contributions proportional to Berry curvature multipoles.

To study the effect of a strong field, we examined the Fourier components of the real-time current (Fig. 5a). We particularly focused on how this real-time SHG response deviates from the second-order perturbation theory. For Fig. 5a, b, we performed the same real-time TDDFT calculation with 100 times stronger field strength than the fields in Fig. 2. While the weak field produces only SHG (see Fig. 2d), the strong field clearly shows up to 8th harmonic generation (8HG) (see Fig. 5b). Hereafter, the n th harmonics are denoted by n HG. The trend of the high harmonics generation (HHG) yields under various ranges of strong fields are plotted in Fig. 5c. In this plot, with the fixed light frequency of $\hbar\omega_0 = 0.52\varepsilon_{\text{gap}}$, we varied the field strength in the window of $0.001 \text{ V \AA}^{-1} \leq E_0 \leq 1.000 \text{ V \AA}^{-1}$, and recorded the HHG yields. The SHG response is not noticeable for the weak fields below 0.001 V \AA^{-1} . Similarly, the 4HG, 6HG, and 8HG yield peaks become significant when the field strength exceeds 0.04, 0.2, and 0.4 V \AA^{-1} , respectively. The logarithmic plot in Fig. 5c shows that the SHG yield follows an apparent quadratic increase ($\propto E_0^2$) with the strengths starting from 0.001 to 0.2 V \AA^{-1} . However, the slope drops for stronger fields, which indicates that the system reaches the nonperturbative limit.

As in Fig. 2e, we compare the theoretical perturbative SHG susceptibility and the SHG yields obtained from the rt-TDDFT calculations. In Fig. 5d, we carried out such a comparison with $E_0 = 0.5 \text{ V \AA}^{-1}$, an exemplary strong field. Unlike the weak field regime example, as can be read from Eq. (15), the SHG yields deviate from the prediction of the perturbation theory. The three-fold symmetry removes the interband BCD ($\mathbf{D}_{vc}^{(2)}$); however, the multipoles ($\mathbf{D}_{vc}^{(4)}, \mathbf{D}_{vc}^{(6)}, \dots$) survive over this symmetry cancellation. Note that the effect of higher poles becomes significant under the strong field. As seen in Fig. 5d, the overall shape of the SHG yield spectrum is mostly consistent with the Berry curvature 4th pole with a marginal difference that can be ascribed to the three-band transition term, as discussed above.

Conclusion

We investigated the second harmonic Hall responses of time-reversal-symmetric insulators in the framework of the real-time propagation of TDDFT and in terms of second-order susceptibility tensor. We found that the SHG susceptibility tensor can be divided into the two-band and the three-band contributions, with the former being proportional to the interband BCD. For a highly symmetric structure, the BCD vanishes due to the cancellation by the mirror reflections, and thus the second harmonic response is wholly governed by the three-band term. For a low symmetry

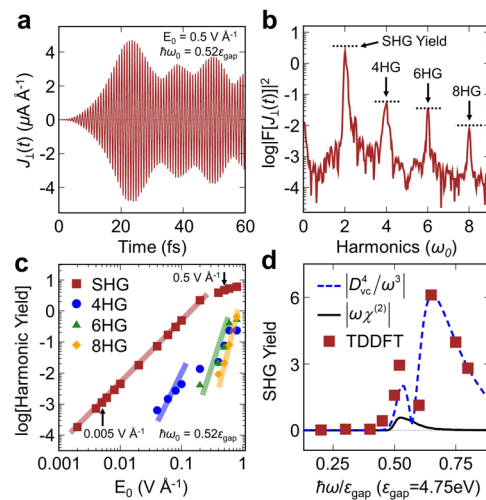


Fig. 5 The second harmonic Hall response to strong fields and contribution of the Berry curvature multipoles.

a The real-time profile of the transverse current density response of the pristine D_{3h} h-BN. The field strength ($E_0 = 0.5 \text{ V \AA}^{-1}$) is 100 times larger than that of Fig. 2c. **b** The Fourier transformation spectra of the current density given in **a** enveloped with a Gaussian function centered at 30 fs with the full-width at half-maximum (FWHM) of 20 fs. The x-axis is scaled with the applied field frequency, $\hbar\omega_0 = 0.52\varepsilon_{\text{gap}}$ (where $\varepsilon_{\text{gap}} = 4.75 \text{ eV}$) and the y-axis is log scaled. Dashed lines and arrows depict the second harmonic generation (SHG) and high harmonic generation (HHG) yields. HHG consists of fourth (4HG), sixth (6HG), and eighth (8HG) harmonic generations. **c** The SHG (brown squares), 4HG (blue circles), 6HG (green triangles), and 8HG (yellow diamonds) yields for various field strengths. Both x and y-axes are log scaled. Arrows show the field strengths used in Fig. 2c-f (0.005 V \AA^{-1}) and panels **a**, **b**, **d** (0.5 V \AA^{-1}). The transparent brown, blue, green, and yellow lines represent the perturbative power rules (E_0^n) for SHG, 4HG, 6HG, and 8HG yield, respectively. **d** is the comparison of the theoretical SHG susceptibility spectra (solid black line) and the SHG yields (brown filled squares) of the transverse current as given in **c** for 0.5 V \AA^{-1} . The blue dashed line is the Berry curvature 4th pole divided by ω^3 , the contribution of high-order corrections to SHG response. The light frequency is scaled with the bandgap.

structure, particularly when the bandgap is small, the BCD term dominates over the second harmonic Hall response of the insulators. We showed that, for a two-band approximated insulator, the higher-order effect of the strong field could be closely associated with the multipoles of the interband Berry curvature. These results of the insulator's Hall response, in terms of interband Berry curvature multipoles, establish a close analogy with the recently recognized formulation of the NLHE in terms of intra-band BCD and multipoles. We suggest that the correspondence between the SHHE and interband BCD can be utilized as SHG-based spectroscopy that can detect insulators' Berry curvature distribution.

Methods

Real-time time-dependent density functional theory calculations. The ground-state electronic structure was obtained by a standard DFT calculation using the Quantum Espresso package⁴³. The preferred exchange and correlation functional was the Perdew–Burke–Ernzerhof-type generalized gradient approximation functional⁴⁴. The scalar-relativistic norm-conserving pseudopotentials were exploited to describe the atomic potentials⁴⁵. The cutoff energy was set as 544 eV. The primitive unit cells with a vacuum slab of 15 \AA were used for the monolayers. The Brillouin zone integration was carried out following a Monkhorst–Pack scheme of $24 \times 24 \times 1$ mesh for time-dependent calculations and $60 \times 60 \times 1$ mesh for static BCD calculations, excluding any symmetry operation. For the computations of the time propagations, we used the plane-wave package developed by our

group⁴⁶, employing the Crank-Nicolson time propagation scheme⁴⁷. The time interval for real-time evolution was set at 0.048 fs.

Data availability

All the obtained numerical data in the present work are available from the corresponding author upon reasonable request.

Code availability

The computation codes used in the present work will be available from the corresponding author upon reasonable request.

Received: 1 June 2022; Accepted: 11 November 2022;

Published online: 26 November 2022

References

- Berry, M. V. Quantal phase-factors accompanying adiabatic changes. *Proc. R. Soc. Lon. Ser. A* **392**, 45–57 (1984).
- Thouless, D. J., Kohmoto, M., Nightingale, M. P. & DenNijs, M. Quantized Hall conductance in a two-dimensional periodic potential. *Phys. Rev. Lett.* **49**, 405–408 (1982).
- Vonklitzing, K., Dorda, G. & Pepper, M. New method for high-accuracy determination of the fine-structure constant based on quantized Hall resistance. *Phys. Rev. Lett.* **45**, 494–497 (1980).
- Liu, C. X., Zhang, S. C. & Qi, X. L. The quantum anomalous Hall effect: theory and experiment. *Annu. Rev. Condens. Matter. Phys.* **7**, 301–321 (2016).
- Hirsch, J. E. Spin Hall effect. *Phys. Rev. Lett.* **83**, 1834–1837 (1999).
- Kane, C. L. & Mele, E. J. Quantum spin Hall effect in graphene. *Phys. Rev. Lett.* **95**, 226801 (2005).
- Shin, D. B. et al. Unraveling materials Berry curvature and Chern numbers from real-time evolution of Bloch states. *Prco. Natl Acad. Sci. USA* **116**, 4135–4140 (2019).
- Xu, S. Y. et al. Discovery of a Weyl fermion semimetal and topological Fermi arcs. *Science* **349**, 613–617 (2015).
- Yan, B. H. & Felsner, C. Topological materials: Weyl semimetals. *Annu. Rev. Condens. Matter. Phys.* **8**, 337–354 (2017).
- Ma, Q. et al. Observation of the nonlinear Hall effect under time-reversal-symmetric conditions. *Nature* **565**, 337–342 (2019).
- Xu, S. Y. et al. Electrically switchable Berry curvature dipole in the monolayer topological insulator WTe₂. *Nat. Phys.* **14**, 900–906 (2018).
- Sodemann, I. & Fu, L. Quantum nonlinear Hall effect induced by Berry curvature dipole in time-reversal invariant materials. *Phys. Rev. Lett.* **115**, 216806 (2015).
- Sipe, J. E. & Shkrebti, A. I. Second-order optical response in semiconductors. *Phys. Rev. B* **61**, 5337–5352 (2000).
- Nastos, F. & Sipe, J. E. Optical rectification and current injection in unbiased semiconductors. *Phys. Rev. B* **82**, 235204 (2010).
- Kim, J. et al. Prediction of ferroelectricity-driven Berry curvature enabling charge- and spin-controllable photocurrent in tin telluride monolayers. *Nat. Commun.* **10**, 3965 (2019).
- Orenstein, J. et al. Topology and symmetry of quantum materials via nonlinear optical responses. *Annu. Rev. Condens. Matter. Phys.* **12**, 247–272 (2021).
- Ma, Q., Grushin, A. G. & Burch, K. S. Topology and geometry under the nonlinear electromagnetic spotlight. *Nat. Mater.* **20**, 1601–1614 (2021).
- de Juan, F., Grushin, A. G., Morimoto, T. & Moore, J. E. Quantized circular photogalvanic effect in Weyl semimetals. *Nat. Commun.* **8**, 15995 (2017).
- Zhang, Y., Sun, Y. & Yan, B. H. Berry curvature dipole in Weyl semimetal materials: an ab initio study. *Phys. Rev. B* **97**, 041101(R) (2018).
- Son, D. T. & Spivak, B. Z. Chiral anomaly and classical negative magnetoresistance of Weyl metals. *Phys. Rev. B* **88**, 104412 (2013).
- Yoda, T., Yokoyama, T. & Murakami, S. Orbital Edelstein effect as a condensed-matter analog of solenoids. *Nano Lett.* **18**, 916–920 (2018).
- Wang, H. & Qian, X. F. Giant optical second harmonic generation in two-dimensional multiferroics. *Nano Lett.* **17**, 5027–5034 (2017).
- Baym G. *Lectures on Quantum Mechanics* (Perseus Books, 1990).
- Patankar, S. et al. Resonance-enhanced optical nonlinearity in the Weyl semimetal TaAs. *Phys. Rev. B* **98**, 165113 (2018).
- Tan, L. Z. & Rappe, A. M. Upper limit on shift current generation in extended systems. *Phys. Rev. B* **100**, 085102 (2019).
- Liu, H. Z. et al. High-harmonic generation from an atomically thin semiconductor. *Nat. Phys.* **13**, 262–265 (2017).
- Luu, T. T. & Werner, H. J. Measurement of the Berry curvature of solids using high-harmonic spectroscopy. *Nat. Commun.* **9**, 916 (2018).
- Holder, T., Kaplan, D. & Yan, B. H. Consequences of time-reversal-symmetry breaking in the light-matter interaction: Berry curvature, quantum metric, and diabatic motion. *Phys. Rev. Res.* **2**, 033100 (2020).
- Kaplan, D., Holder, T. & Yan, B. H. Nonvanishing subgap photocurrent as a probe of lifetime effects. *Phys. Rev. Lett.* **125**, 227401 (2020).
- Matsyshyn, O. & Sodemann, I. Nonlinear Hall acceleration and the quantum rectification sum rule. *Phys. Rev. Lett.* **123**, 246602 (2019).
- You, J. S., Fang, S., Xu, S. Y., Kaxiras, E. & Low, T. Berry curvature dipole current in the transition metal dichalcogenides family. *Phys. Rev. B* **98**, 121109(R) (2018).
- Gao, Y., Yang, S. A. & Niu, Q. Field induced positional shift of Bloch electrons and its dynamical implications. *Phys. Rev. Lett.* **112**, 166601 (2014).
- Wang, C., Gao, Y. & Xiao, D. Intrinsic nonlinear Hall effect in antiferromagnetic tetragonal CuMnAs. *Phys. Rev. Lett.* **127**, 277201 (2021).
- Liu, H. Y. et al. Intrinsic second-order anomalous Hall effect and its application in compensated antiferromagnets. *Phys. Rev. Lett.* **127**, 277202 (2021).
- Lai, S. et al. Third-order nonlinear Hall effect induced by the Berry-connection polarizability tensor. *Nat. Nanotechnol.* **16**, 869–873 (2021).
- Liu, H. Y. et al. Berry connection polarizability tensor and third-order Hall effect. *Phys. Rev. B* **105**, 045118 (2022).
- He, P. et al. Quantum frequency doubling in the topological insulator Bi₂Se₃. *Nat. Commun.* **12**, 698 (2021).
- Mao-Sen, Q. et al. Strain tunable Berry curvature dipole, orbital magnetization and nonlinear Hall effect in WSe₂ monolayer. *Chin. Phys. Lett.* **38**, 017301 (2021).
- Zhang, C. P., Gao, X. J., Xie, Y. M., Po, H. C. & Law, K. T. Higher-order nonlinear anomalous Hall effects induced by Berry curvature multipoles. Preprint at *arXiv* 2012.15628 (2021).
- Ahn, J., Guo, G. Y., Nagaosa, N. & Vishwanath, A. Riemannian geometry of resonant optical responses. *Nat. Phys.* **18**, 290–296 (2022).
- Rhodes, W. & Chase, M. Generalized susceptibility theory. I. Theories of hypochromism. *Rev. Mod. Phys.* **39**, 348 (1967).
- Pan, L. W., Taylor, K. T. & Clark, C. W. Perturbation-theory study of high-harmonic generation. *J. Opt. Soc. Am. B* **7**, 509–516 (1990).
- Giannozzi, P. et al. Quantum espresso: a modular and open-source software project for quantum simulations of materials. *J. Phys. Condens. Matter.* **21**, 395502 (2009).
- Perdew, J. P., Burke, K. & Ernzerhof, M. Generalized gradient approximation made simple. *Phys. Rev. Lett.* **77**, 3865 (1996).
- Hamann, D. R. Optimized norm-conserving Vanderbilt pseudopotentials. *Phys. Rev. B* **88**, 085117 (2013).
- Shin, D., Lee, G., Miyamoto, Y. & Park, N. Real-time propagation via time-dependent density functional theory plus the Hubbard U potential for electron-atom coupled dynamics involving charge transfer. *J. Chem. Theory Comput.* **12**, 201–208 (2016).
- Crank, J. & Nicolson, P. A practical method for numerical evaluation of solutions of partial differential equations of the heat-conduction type. *Adv. Comput. Math.* **6**, 207–226 (1996).

Acknowledgements

This work was supported by the National Research Foundation of Korea (NRF) grant (No. NRF-2019R1A2C2089332) funded by the Korean government (MSIT). K.W.K. acknowledges financial support from Basic Science Research Program through NRF funded by the Ministry of Education (20211060) and MSIT (No.2020R1A5A1016518). H.J. was supported by NRF under grants 2021M3H4A1A03054864 and 2019R1A2C1010498. B.Y. acknowledges the financial support from the European Research Council (ERC Consolidator Grant “NonlinearTopo”, No. 815869). We thank Prof. Angel Rubio and Dr Nicolas Tancogne-Dejean from the Max Planck Institute for the Structure and Dynamics of Matter, and Dr Kyoung-Whan Kim from the Korea Institute of Science and Technology for valuable and productive discussions.

Author contributions

M.S.O. performed ab initio calculations, developed the model Hamiltonian code, and analyzed the data. M.S.O. and N.P. constructed the manuscript. S.A.S., K.W.K., B.Y., and H.J. helped to strengthen the discussion. All authors analyzed the results and contributed to the manuscript.

Competing interests

The authors declare no competing interests.

Additional information

Supplementary information The online version contains supplementary material available at <https://doi.org/10.1038/s42005-022-01086-9>.

Correspondence and requests for materials should be addressed to Noejung Park.

Peer review information *Communications Physics* thanks Tran Trung Luu and the other, anonymous, reviewer(s) for their contribution to the peer review of this work. Peer reviewer reports are available.

Reprints and permission information is available at <http://www.nature.com/reprints>

Publisher's note Springer Nature remains neutral with regard to jurisdictional claims in published maps and institutional affiliations.



Open Access This article is licensed under a Creative Commons Attribution 4.0 International License, which permits use, sharing, adaptation, distribution and reproduction in any medium or format, as long as you give appropriate credit to the original author(s) and the source, provide a link to the Creative Commons license, and indicate if changes were made. The images or other third party material in this article are included in the article's Creative Commons license, unless indicated otherwise in a credit line to the material. If material is not included in the article's Creative Commons license and your intended use is not permitted by statutory regulation or exceeds the permitted use, you will need to obtain permission directly from the copyright holder. To view a copy of this license, visit <http://creativecommons.org/licenses/by/4.0/>.

© The Author(s) 2022